This is an author-deposited version published in: https://sam.ensam.eu
Handle ID: .http://hdl.handle.net/10985/26063

To cite this version :

Flora LAHOUZE, Wahbi JOMAA, Cyrille MÉTAYER, Francesco PANERAI, Jean LACHAUD - Pyromechanics: A solid mechanics approach to deformation during pyrolysis - Fuel - Vol. 390, - 2025

Fuel 390 (2025) 134557

Contents lists available at ScienceDirect

Fuel

journal homepage: www.elsevier.com/locate/fuel

Full length article

Pyromechanics: A solid mechanics approach to deformation during pyrolysis

Flora Lahouze [a,b,*], Wahbi Jomaa [a,b], Cyrille Métayer [c], Michaël Meyer [c], Francesco Panerai [d,e], Jean Lachaud [a,b]

[a] Univ. Bordeaux, CNRS, Bordeaux INP, I2M, UMR 5295, F-33400 Talence, France
[b] Arts et Metiers Institute of Technology, CNRS, Bordeaux INP, I2M, UMR 5295, F-33400 Talence, France
[c] Institut des Sciences Exactes et Appliquées-EA 7484, Université de la Nouvelle-Calédonie, Nouméa, 98851, France
[d] Center for Hypersonics and Entry Systems Studies, University of Illinois at Urbana-Champaign, Urbana, 61801, IL, USA
[e] Department of Aerospace Engineering, University of Illinois at Urbana-Champaign, Urbana, 61801, IL, USA

ARTICLE INFO

Keywords:
Biomass pyrolysis
Shrinkage
Mechanics
Anisotropy

ABSTRACT

During pyrolysis, organic materials undergo morphological changes that are important to predict, particularly in the field of thermochemical conversion. This work proposes an approach to model deformations during pyrolysis combining elastic, thermal expansion, and pyrolysis contributions. A three-dimensional anisotropic pyromechanics model is derived for porous media by volume averaging. It includes pyrolysis kinetics, mass, momentum and energy conservation for both solid and gas phases. A key advantage of the pyromechanics model lies in its physical framework, which effectively captures the effect of internal stresses on the overall deformation. Implemented as open-source within the Porous material Analysis Toolbox based on the OpenFOAM framework (PATO) using an incremental approach, the model is specifically applied to wood in this study. Two experimental validations are conducted using pyrolyzing cylindrical wood particles to verify the model's predictions concerning temperature profile evolution and shrinkage effects. Importantly, the model's capability to estimate stress distribution holds promise for further investigations into crack distribution and propagation.

1. Introduction

Pyrolysis of wood and other organic solid materials is a key process in the development of sustainable fuels and valuable energy products [1]. Occurring at temperatures above 250 °C, pyrolysis plays a crucial role in thermochemical conversion processes that transform biomass into a range of high-value products, including hydrogen and biochar. This thermochemical degradation is a multi-physics and multi-scale problem. Researchers have primarily focused on studying thermophysical phenomena such as pyrolysis kinetics, heat, and mass transfer. However, pyrolysis inherently involves shrinkage, which alters heat transfer by modifying characteristic lengths and volume [2–4]. Such volume loss impacts conversion time and final products yields in the thermally thick regime (Bi > 10) [2,5]. Additionally, the stresses induced by these structural changes may lead to crack formation both in depth and at the surface [5–7]. Therefore, understanding this mechanical behavior is essential for accurately describing pyrolysis processes. By analogy with the term thermomechanics, which describes the behavior of materials related to thermal expansion, the term pyromechanics is used to describe the behavior of pyrolyzing materials that undergo additional dimensional changes as a result of chemical transformations.

The first models accounting for shrinkage emerged in the 1980s. One of the earliest comprehensive models accounting for both shrinkage and expansion during pyrolysis was developed by J. B. Henderson and T. E. Wiecek in 1987 [8]. Their one-dimensional transient thermal model considered not only decomposition but also thermochemical expansion and shrinkage in polymer composites exposed to high temperatures. J. Villermaux et al. [9] proposed a model for fast pyrolysis of solid particles including shrinkage through a linear shrinking velocity, assuming a constant density and a one-step pyrolysis model. C. Di Blasi [3] began to vary density by introducing a model determined by empirical correlations. This model assumes that the volume occupied by the solid decreases linearly with solid mass and increases with char mass, driven by a shrinkage factor [3,10,11]. As an alternative to working with the volume, some authors define a shrinkage factor as the ratio between the local length of the pyrolyzing particle and its initial length, varying linearly with the conversion [12] or non-linearly [13]. While these approaches improved physical realism, it was limited to one dimensional isotropic behavior. Recently, researchers have highlighted the importance of considering the anisotropic properties of biomass in thermochemical conversion processes. M. Sánchez

---

[*] Corresponding author at: Univ. Bordeaux, CNRS, Bordeaux INP, I2M, UMR 5295, F-33400 Talence, France.
E-mail address: flora.lahouze@u-bordeaux.fr (F. Lahouze).

https://doi.org/10.1016/j.fuel.2025.134557
Received 18 November 2024; Received in revised form 16 January 2025; Accepted 29 January 2025

Nomenclature

Latin

$\mathcal{A}_{ij}$	Arrhenius law pre-exponential factor of pyrolysis reaction j of component i $\mathrm{s^{-1}}$
$\mathcal{E}_{ij}$	Arrhenius law activation energy of pyrolysis reaction j of component i $\mathrm{J\,mol^{-1}}$
$\mathcal{F}_{ij}$	Mass loss fraction of component i by pyrolysis reaction j
$\mathbf{n}$	Unit normal vector
$\mathbf{u}$	Solid displacement m
$\mathbf{v_b}$	Mesh velocity $\mathrm{m\,s^{-1}}$
$\mathbf{v_g}$	Gaseous velocity $\mathrm{m\,s^{-1}}$
$\mathbf{v_s}$	Solid velocity $\mathrm{m\,s^{-1}}$
$\underline{\underline{\mathbf{K}}}$	Permeability tensor $\mathrm{m^2}$
$\underline{\underline{\underline{\underline{\mathbf{C}}}}}$	Rigidity tensor Pa
$\underline{\underline{\mathbf{k}}}$	Solid conductivity tensor $\mathrm{W\,m^{-1}\,K^{-1}}$
c_p	Thermal capacity $\mathrm{J\,kg^{-1}\,K^{-1}}$
E	Young modulus Pa
e_g	Total gaseous energy $\mathrm{J\,m^{-3}}$
e_s	Total solid energy $\mathrm{J\,m^{-3}}$
G	Shear modulus Pa
h_f	Standard formation enthalpy $\mathrm{J\,kg^{-1}}$
h_g	Gaseous enthalpy $\mathrm{J\,kg^{-1}}$
h_i	Solid component i enthalpy $\mathrm{J\,kg^{-1}}$
M_g	Gaseous molar mass $\mathrm{kg\,kmol^{-1}}$
N_p	Number of solid components
p_g	Gaseous pressure Pa
P_i	Number of pyrolysis reactions for component i
R	Universal gas constant $\mathrm{J\,K^{-1}\,kmol^{-1}}$
T	Temperature K
V	Volume $\mathrm{m^3}$

Greek

χ_{ij}	Advancement of pyrolysis reaction j of component i
ϵ_g	Gaseous volume fraction
ϵ_i	Solid component i volume fraction
μ_g	Gas viscosity $\mathrm{Pa\,s}$
ν	Poisson coefficient
π_{tot}	Total pyrolysis production rate $\mathrm{kg\,m^{-3}\,s^{-1}}$
ψ	Generic variable
ρ_g	Gaseous density $\mathrm{kg\,m^{-3}}$
ρ_i	Solid component i density $\mathrm{kg\,m^{-3}}$
ρ_s	Solid phase density $\mathrm{kg\,m^{-3}}$
τ	Total average pyrolysis advancement
$\underline{\underline{\alpha}}$	Thermal expansion tensor $\mathrm{K^{-1}}$
$\underline{\underline{\sigma}}$	Cauchy stress tensor Pa
$\underline{\underline{\epsilon}}$	Strain tensor
$\underline{\underline{\xi}}$	Pyrolysis shrinkage tensor

Conventions

$\langle\rangle^g$	Intrinsic gas phase average
$\langle\rangle^s$	Intrinsic solid phase average
$\langle\rangle$	Phase average
$\nabla\cdot$	Divergence $\mathrm{m^{-1}}$
∇	Gradient $\mathrm{m^{-1}}$
$\cdot$	Scalar product

et al. [14] demonstrated that anisotropy in thermal conductivity and permeability significantly affects the prediction of mass loss. B. Pecha et al. [15] showed that incorporating anisotropic permeability impacts conversion times, especially for Biot numbers greater than 0.1. F. Li et al. [16] further demonstrated that the combined influence of thermal conductivity, permeability, and shrinkage anisotropy plays a critical role in conversion, with shrinkage anisotropy emerging as a key factor in shaping biomass pyrolysis behavior. To address anisotropy, M. Bellais [17] introduced three shrinkage sub-models for anisotropic materials: uniform shrinkage, shrinking shell model and shrinking cylinder model. These sub-models were introduced to offer several methods of averaging conversion to avoid meshing problems. As demonstrated by J. Blondeau et al. [18], averaging can introduce an artificial shrinkage in areas where conversion has not yet begun, thus modifying the apparent density. Moving beyond shrinkage, some authors investigated stress development as a consequence of the degradation of mechanical-properties [6,7,19]. To our knowledge, the most advanced models are the 2D-cylindrical one of M. Sreekanth et al. [20] and the 3D isotropic one of J. Wang et al. [21], which account for shrinkage-induced stresses during drying and pyrolysis. Nevertheless, these models are either isotropic or restricted to 2D geometries. Only few authors have gone as far as studying cracking through stress concentrations [20,22,23].

This work introduces a 3D anisotropic pyromechanics model accounting for the coupled effects of shrinkage, heat and mass transfer, and stress generation. This model provides a detailed description of deformation mechanisms—including elastic, thermal expansion, and pyrolysis-induced strains—and enables the computation of stress distributions, essential for cracking analysis.

The article is structured as follows. In Section 2, we present the governing equations of the 3D pyromechanics model. In Section 3 we propose an efficient numerical approach and describe its implementation in the Porous material Analysis Toolbox based on OpenFOAM (PATO) software [24]. Finally, in Section 4 we apply the model and numerical method to analyze two pyrolysis experiments carried out on cylindrical wood particles. We present a detailed reconstruction of mass loss, temperature profile, local stresses, and overall deformation.

2. Governing equations

We present in this section the governing equations of the pyromechanics model. It consists of a set of conservation equations applied to a multiphasic porous medium, containing a gas phase and a solid phase, using the volume-averaging approach [25]. In this work, the solid phase is decomposed into four reacting components which are the three main components of the wood cell wall (cellulose, hemicellulose and lignin) and water, as illustrated in Fig. 1. Additionally, wood is considered as a deformable porous medium.

2.1. Hypothesis and notations

Consider ψ_i a local value of a physical variable defined in the gas phase ($i = g$) or in the solid phase ($i = s$). Following the volume-averaging approach, phase variables are defined as

$$\langle\psi_i\rangle = \langle\psi_i(\mathbf{x},t)\rangle = \frac{1}{V}\int_{V_i}\psi_i(\mathbf{x}+\mathbf{y},t)\,dV, \tag{1}$$

and intrinsic phase variables are defined as

$$\langle\psi_i\rangle^i = \langle\psi_i(\mathbf{x},t)\rangle^i = \frac{1}{V_i}\int_{V_i}\psi_i(\mathbf{x}+\mathbf{y},t)\,dV, \tag{2}$$

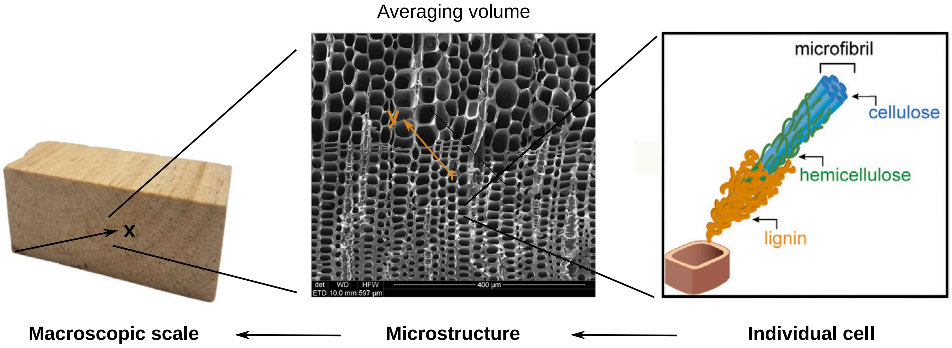

Fig. 1. Illustration of the multi-scale nature of wood and major cell wall components (adapted from [26]). Notation for the three-dimensional space coordinates used in the volume averaging approach: **x**: macroscopic scale, **y**: local scale.

where **x** is the macroscopic coordinate and **y** is the local coordinate within the averaging volume V, as schematized in Fig. 1, and V_i is the volume of phase i within the averaging volume.

The volume fraction of each phase i is then expressed as

$$\langle \psi_i \rangle = \epsilon_i \langle \psi_i \rangle^i. \tag{3}$$

For example, the volume averaged total density $\langle \rho \rangle$ of wood material, filled with gas and a solid phase containing N_p solid components, is given by

$$\langle \rho \rangle = \langle \rho_g \rangle + \langle \rho_s \rangle = \epsilon_g \langle \rho_g \rangle^g + \sum_{i \in [1, N_p]} \epsilon_i \langle \rho_i \rangle^i. \tag{4}$$

2.2. Pyrolysis

The chosen kinetic model assumes that the solid components i may decompose following P_i pyrolysis reactions, resulting in the production of char and gas. For a more detailed development, particularly regarding a material chemistry model accounting for the generation of species and/or elements, readers are referred to [25].

The advancement χ_{ij} (varying from 0 to 1) of the pyrolysis reaction j of component i is modeled using Arrhenius laws of the general form

$$\frac{\partial_t \chi_{ij}}{(1 - \chi_{ij})} = \mathcal{A}_{ij} \exp\left(-\frac{\mathcal{E}_{ij}}{RT}\right), \quad \forall i \in [1, N_p], \forall j \in [1, P_i]. \tag{5}$$

where N_p is the number of components and P_i is the number of pyrolysis reactions of component i. $\mathcal{A}_{ij}$ and $\mathcal{E}_{ij}$ are respectively the pre-exponential factor and energy activation of pyrolysis reaction j of component i. The apparent density of component i is then updated as

$$\frac{\epsilon_i \langle \rho_i \rangle^i}{\epsilon_{i,0} \ \langle \rho_{i,0} \rangle^i} = 1 - \sum_{j \in [1, P_i]} \mathcal{F}_{ij} \chi_{ij}, \tag{6}$$

where $\epsilon_{i,0}$, $\langle \rho_{i,0} \rangle^i$, and $\mathcal{F}_{ij}$, are respectively the initial (at $t = 0$) volume fraction of component i, intrinsic virgin density of component i, and mass loss fraction of component i by pyrolysis reaction j. The total average pyrolysis advancement, varying from 1 to 0, is obtained as

$$\tau = \sum_{i \in [1, N_p]} \sum_{j \in [1, P_i]} \frac{\epsilon_{i,0} \ \langle \rho_{i,0} \rangle^i \ \mathcal{F}_{ij}}{\sum_{i \in [1, N_p]} \sum_{j \in [1, P_i]} \epsilon_{i,0} \ \langle \rho_{i,0} \rangle^i \ \mathcal{F}_{ij}} \ (1 - \chi_{ij}). \tag{7}$$

2.3. Mass conservation

2.3.1. Gas phase

Mass conservation for the gas phase includes the overall pyrolysis gas production rate π_{tot} with no consideration of heterogeneous reactions as

$$\partial_t \left(\epsilon_g \langle \rho_g \rangle^g \right) + \nabla \cdot \left(\epsilon_g \langle \rho_g \rangle^g \langle \mathbf{v_g} \rangle^g \right) = \pi_{tot}. \tag{8}$$

π_{tot} is obtained by summation of the gas productions of the N_p solid components and reads

$$\pi_{tot} = \sum_{i \in [1, N_p]} \sum_{j \in [1, P_i]} \epsilon_{i,0} \ \langle \rho_{i,0} \rangle^i \ \mathcal{F}_{ij} \ \partial_t \chi_{ij}. \tag{9}$$

The gas volume fraction ϵ_g is equivalent to wood porosity and computed as $\epsilon_g = 1 - \sum_{i \in [1, N_p]} \epsilon_i$.

2.3.2. Solid phase

The total average solid mass evolution is obtained as

$$\partial_t(\langle \rho_s \rangle) + \nabla \cdot \left(\langle \rho_s \rangle \langle \mathbf{v_s} \rangle^s \right) = -\pi_{tot}. \tag{10}$$

where $\langle \mathbf{v_s} \rangle^s$ denotes the intrinsic average velocity of the solid phase. The special numerical treatment of this solid velocity is detailed in Section 3.

2.4. Momentum conservation

2.4.1. Gas phase

In deformable porous media, the volume-averaged momentum conservation may be written as [27,28]

$$\langle \mathbf{v_g} \rangle^g = -\left(\frac{1}{\epsilon_g \mu_g} \underline{\underline{\mathbf{K}}} \right) \cdot \nabla \langle p_g \rangle^g + \langle \mathbf{v_s} \rangle^s, \tag{11}$$

with μ_g the gas viscosity, $\underline{\underline{\mathbf{K}}}$ the permeability tensor and $\langle p_g \rangle^g$ the gas pressure.

By assuming the perfect gas law holds,

$$\langle \rho_g \rangle^g = \frac{M_g \langle p_g \rangle^g}{R \langle T \rangle}, \tag{12}$$

the average gas velocity is obtained by resolution of the momentum-conservation equation by assembling Eqs. (8), (11) and (12),

$$\partial_t \left(\frac{\epsilon_g M_g}{R \langle T \rangle} \langle p_g \rangle^g \right) + \nabla \cdot \left(\frac{M_g}{R \langle T \rangle} \langle p_g \rangle^g \left[\left(-\frac{1}{\mu_g} \underline{\underline{\mathbf{K}}} \right) \cdot \nabla \langle p_g \rangle^g + \langle \mathbf{v_s} \rangle^s \right] \right) = \pi^{tot}. \tag{13}$$

M_g is the gas molar mass, R the universal gas constant and $\langle T \rangle$ the average temperature. All the thermophysical gas properties are tabulated as a function of the average temperature.

2.4.2. Solid phase

The mechanical part of the model presented here introduces stress and strain analysis to existing shrinkage models. Thermal expansion and pyrolysis shrinkage occur in solid parts undergoing decomposition. The strain field caused by these processes is not geometrically consistent with the structure of solid regions that have not yet experienced pyrolysis. Consequently, a mechanical strain tensor arises. This model thus accounts for the stresses related to this strain field. However, this study does not address the full poroelasticity problem, as it excludes stresses from interactions between the gas and solid phases.

The response of the material will be assumed to be purely elastic, with the assumptions of small perturbations between two close states. Therefore, we can introduce the Cauchy stress tensor $\underline{\underline{\boldsymbol{\sigma}}}$, defined in the current configuration, and the linearized strain tensor $\underline{\underline{\boldsymbol{\varepsilon}}}$.

The momentum conservation of the solid phase is written as

$$\partial_t \left(\langle \rho_s \rangle \partial_t \langle \mathbf{u} \rangle^s \right) - \nabla \cdot \langle \underline{\underline{\boldsymbol{\sigma}}} \rangle^s = \mathbf{0}. \tag{14}$$

with $\langle \mathbf{u} \rangle^s$ the macroscopic solid displacement and $\langle \underline{\underline{\boldsymbol{\sigma}}} \rangle^s$ the macroscopic Cauchy stress tensor.

Following the work done for the drying of shrinking materials [29, 30], the total strain of the solid phase is the sum of the mechanical, thermal and pyrolysis shrinkage contributions as

$$\langle \underline{\underline{\boldsymbol{\varepsilon}}} \rangle^s = \langle \underline{\underline{\boldsymbol{\varepsilon}}}^{el} \rangle^s + \langle \underline{\underline{\boldsymbol{\varepsilon}}}^{th} \rangle^s + \langle \underline{\underline{\boldsymbol{\varepsilon}}}^{sh} \rangle^s, \tag{15}$$

where $\langle \underline{\underline{\boldsymbol{\varepsilon}}}^{el} \rangle^s$, $\langle \underline{\underline{\boldsymbol{\varepsilon}}}^{th} \rangle^s$ and $\langle \underline{\underline{\boldsymbol{\varepsilon}}}^{sh} \rangle^s$ are respectively the elastic, the thermal expansion and the pyrolysis shrinkage parts of the strain tensor.

The relation between the total strain and the displacement $\langle \mathbf{u} \rangle^s$ is written as

$$\langle \underline{\underline{\boldsymbol{\varepsilon}}} \rangle^s = \frac{1}{2} \left(\nabla \langle \mathbf{u} \rangle^s + \nabla \langle \mathbf{u} \rangle^{sT} \right). \tag{16}$$

Finally, a linear elastic anisotropic constitutive law is written in terms of the macroscopic fourth order rigidity tensor $\langle \underline{\underline{\underline{\underline{\mathbf{C}}}}} \rangle$ as

$$\langle \underline{\underline{\boldsymbol{\sigma}}} \rangle^s = \langle \underline{\underline{\underline{\underline{\mathbf{C}}}}} \rangle : \langle \underline{\underline{\boldsymbol{\varepsilon}}}^{el} \rangle^s = \langle \underline{\underline{\underline{\underline{\mathbf{C}}}}} \rangle : \left(\langle \underline{\underline{\boldsymbol{\varepsilon}}} \rangle^s - \langle \underline{\underline{\boldsymbol{\varepsilon}}}^{th} \rangle^s - \langle \underline{\underline{\boldsymbol{\varepsilon}}}^{sh} \rangle^s \right). \tag{17}$$

Considering wood as an orthotropic material, the total volumetric thermal expansion and shrinkage are distributed unequally for the three orthotropic principal directions. These directions illustrated on Fig. 2 are referred to as tangential $(1, T, x)$, radial $(2, R, y)$ and longitudinal $(3, L, z)$. As a consequence, we assume the macroscopic thermal expansion tensor $\langle \underline{\underline{\boldsymbol{\alpha}}} \rangle$ and macroscopic pyrolysis shrinkage tensor $\langle \underline{\underline{\boldsymbol{\xi}}} \rangle$ composed of linear coefficients,

$$\langle \underline{\underline{\boldsymbol{\alpha}}} \rangle = \begin{bmatrix} \alpha_{11} & 0 & 0 \\ 0 & \alpha_{22} & 0 \\ 0 & 0 & \alpha_{33} \end{bmatrix} \text{ and } \langle \underline{\underline{\boldsymbol{\xi}}} \rangle = \begin{bmatrix} \xi_{11} & 0 & 0 \\ 0 & \xi_{22} & 0 \\ 0 & 0 & \xi_{33} \end{bmatrix}. \tag{18}$$

During thermal expansion, the lengths are assumed to vary linearly with the temperature. Similarly during pyrolysis, the lengths are assumed to vary linearly with the pyrolysis advancement. The thermal expansion and the pyrolysis shrinkage strains are then expressed as

$$\langle \underline{\underline{\boldsymbol{\varepsilon}}}^{th} \rangle^s = \langle \underline{\underline{\boldsymbol{\alpha}}} \rangle (T - T_0) \quad \text{and} \quad \langle \underline{\underline{\boldsymbol{\varepsilon}}}^{sh} \rangle^s = \langle \underline{\underline{\boldsymbol{\xi}}} \rangle (\tau - \tau_0), \tag{19}$$

and the detailed expression of Eq. (17) is

$$\langle \underline{\underline{\boldsymbol{\sigma}}} \rangle^s = \langle \underline{\underline{\underline{\underline{\mathbf{C}}}}} \rangle : \left(\frac{1}{2} \left[\nabla \langle \mathbf{u} \rangle^s + (\nabla \langle \mathbf{u} \rangle^s)^{\mathrm{T}} \right] - \langle \underline{\underline{\boldsymbol{\alpha}}} \rangle (T - T_0) - \langle \underline{\underline{\boldsymbol{\xi}}} \rangle (\tau - \tau_0) \right). \tag{20}$$

This constitutive law introduces an irreversible behavior through dependence on pyrolysis advancement. For an orthotropic material, the rigidity tensor $\langle \underline{\underline{\underline{\underline{\mathbf{C}}}}} \rangle$ can be written in matrix form as

$$\langle \underline{\underline{\underline{\underline{\mathbf{C}}}}} \rangle = \begin{bmatrix} C_{11} & C_{12} & C_{13} & 0 & 0 & 0 \\ C_{12} & C_{22} & C_{23} & 0 & 0 & 0 \\ C_{13} & C_{23} & C_{33} & 0 & 0 & 0 \\ 0 & 0 & 0 & C_{44} & 0 & 0 \\ 0 & 0 & 0 & 0 & C_{55} & 0 \\ 0 & 0 & 0 & 0 & 0 & C_{66} \end{bmatrix}. \tag{21}$$

This tensor is composed of 12 material constants (Young modulus E_i, Poisson coefficients ν_{ij} and shear modulus G_{ij} for $i, j = 1, 2, 3$) and 9 independent coefficients C_{ij} with the relation $\nu_{ij} = \nu_{ji} \frac{E_i}{E_j}$ [31]. Introducing the constant J as

$$J = \frac{1 - \nu_{12}\nu_{21} - \nu_{23}\nu_{32} - \nu_{31}\nu_{13} - 2\nu_{21}\nu_{32}\nu_{13}}{E_1 E_2 E_3}, \tag{22}$$

the coefficients C_{ij} are written as

$$\begin{aligned} C_{11} &= \frac{1}{J} \frac{1 - \nu_{23}\nu_{32}}{E_2 E_3} & C_{12} &= \frac{1}{J} \frac{\nu_{12} + \nu_{32}\nu_{13}}{E_1 E_3} & C_{31} &= \frac{1}{J} \frac{\nu_{31} + \nu_{21}\nu_{32}}{E_2 E_3} \\ C_{22} &= \frac{1}{J} \frac{1 - \nu_{13}\nu_{31}}{E_1 E_3} & C_{23} &= \frac{1}{J} \frac{\nu_{23} + \nu_{21}\nu_{13}}{E_1 E_2} & C_{33} &= \frac{1}{J} \frac{1 - \nu_{21}\nu_{12}}{E_2 E_1} \\ C_{44} &= 2G_{12} & C_{55} &= 2G_{23} & C_{66} &= 2G_{31}. \end{aligned} \tag{23}$$

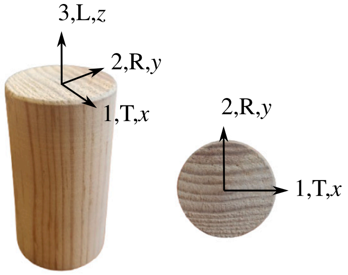

Fig. 2. Orthotropic principal coordinate system for wood.

2.5. Energy conservation

Considering local thermal equilibrium ($\langle T_g \rangle = \langle T_s \rangle = \langle T \rangle$) between the gas phase and the solid phase, the energy conservation may be written as

$$\sum_{i \in [1, N_p]} \partial_t (\epsilon_i \langle \rho_i \rangle^i \langle h_i \rangle^i) + \partial_t \left(\epsilon_g \langle \rho_g \rangle^g \langle e_g \rangle^g \right) = \begin{cases} \nabla \cdot \left(\underline{\underline{\mathbf{k}}} \, \nabla \langle T \rangle \right) \\ -\nabla \cdot \left(\epsilon_g \langle \rho_g \rangle^g \langle h_g \rangle^g \langle \mathbf{v_g} \rangle^g \right) \\ -\nabla \cdot \left(\sum_{i \in [1, N_p]} \epsilon_i \langle \rho_i \rangle^i \langle h_i \rangle^i \langle \mathbf{v_s} \rangle^s \right) \end{cases} \tag{24}$$

The left-hand side is composed by the solid and gaseous storage. By neglecting the solid pressure variations, the solid storage is expressed as

$$\sum_{i \in [1, N_p]} \partial_t (\epsilon_i \langle \rho_i \rangle^i \langle h_i \rangle^i) = \sum_{i \in [1, N_p]} \left[\epsilon_i \langle \rho_i \rangle^i c_{p,i} \partial_t T + \langle h_i \rangle^i \partial_t (\epsilon_i \langle \rho_i \rangle^i) \right], \tag{25}$$

and the gaseous storage is expressed as

$$\partial_t \left(\epsilon_g \langle \rho_g \rangle^g \langle e_g \rangle^g \right) = \partial_t \left(\epsilon_g \langle \rho_g \rangle^g \langle h_g \rangle^g - \epsilon_g \langle p_g \rangle^g \right). \tag{26}$$

The right-hand side of Eq. (24) is composed by the solid thermal conduction, the gaseous and the solid thermal convection. The effective conductivity $\underline{\underline{\mathbf{k}}}$ is a second order tensor, accounting for conduction in the solid, conduction in the gas, radiative heat transfer and dispersion. Eq. (24) is then written as

$$\sum_{i \in [1, N_p]} (\epsilon_i \langle \rho_i \rangle^i \langle c_{p,i} \rangle^i) \partial_t \langle T \rangle + \partial_t \left(\epsilon_g \langle \rho_g \rangle^g \langle h_g \rangle^g - \epsilon_g \langle p_g \rangle^g \right) = \begin{cases} \nabla \cdot \left(\underline{\underline{\mathbf{k}}} \, \nabla \langle T \rangle \right) \\ -\nabla \cdot \left(\epsilon_g \langle \rho_g \rangle^g \langle h_g \rangle^g \langle \mathbf{v_g} \rangle^g \right) \\ -\nabla \cdot \left(\sum_{i \in [1, N_p]} \epsilon_i \langle \rho_i \rangle^i \langle h_i \rangle^i \langle \mathbf{v_s} \rangle^s \right) \\ - \sum_{i \in [1, N_p]} \langle h_i \rangle^i \partial_t (\epsilon_i \langle \rho_i \rangle^i) \end{cases} \tag{27}$$

The solid enthalpies $\langle h_i \rangle^i$ are the sum of the standard formation enthalpy of functional polymer group j of solid component i at the reference temperature $T_0 = 298.15$ K, $h_{f,ij}$, and the sensible enthalpy required to bring the component i from temperature T_0 to T [32],

$$\langle h_i \rangle^i = \sum_{j\in[1,P_i]} h_{f,ij} + \int_{T_0}^{T} c_{p,i}\, dT. \tag{28}$$

3. Numerical model

The simulation domain and the governing equations are discretized using a second order finite volume procedure and solved within the Porous material Analysis Toolbox based on OpenFOAM (PATO) [24]. This section presents the numerical strategy used to manage large displacements.

3.1. Incremental approach

For thermally thick regimes, the thermal problem is intrinsically transient. Therefore, it is necessary to account for this time dependency when studying the structural changes. Furthermore, macroscopic displacement related to shrinkage during pyrolysis are known to be large, wood can loose up to 70% of its volume [4]. The material points of the solid undergo significant changes of position during pyrolysis shrinkage. The mechanical problem therefore involves geometric non-linearities (large displacements). When the initial and last configurations can no longer be confused, it becomes necessary to use non-linear formalisms [33].

In this work, the first step is to keep a linear formalism by considering successive quasi-static states and by solving the mathematical model with an incremental approach, illustrated on Fig. 3. This approach preserves the framework of the superposition principle, namely the linearity of the constitutive law and the ability to sum the different effects of small deformations.

The numerical time step dt is introduced as an increment for the equilibrium states. Any variable ψ^{t+dt} of the current configuration is expressed as

$$\psi^{t+dt} = \psi^t + \delta\psi, \tag{29}$$

with ψ^t the variable in the last configuration and $\delta\psi$ the small increment between times t and $t + dt$.

For successive equilibrium states, Eq. (14) for momentum conservation is written as

$$\nabla \cdot (\underline{\underline{\boldsymbol{\sigma}}}^{t+dt}) = \nabla \cdot (\underline{\underline{\boldsymbol{\sigma}}}^{t} + \delta\underline{\underline{\boldsymbol{\sigma}}}) = \mathbf{0}. \tag{30}$$

Considering that the state at previous time is the reference state, we write that at time t, $\nabla \cdot \underline{\underline{\boldsymbol{\sigma}}}^{t} = \mathbf{0}$ is verified. Eq. (30) becomes

$$\nabla \cdot \delta\underline{\underline{\boldsymbol{\sigma}}} = \mathbf{0},\ \forall t, \tag{31}$$

with the constitutive law expressed as

$$\delta\underline{\underline{\boldsymbol{\sigma}}} = \langle \underline{\underline{\underline{\mathbf{C}}}} \rangle : \left(\frac{1}{2} \left[\nabla(\delta\mathbf{u}) + (\nabla(\ \delta\mathbf{u})\ )^{\mathrm{T}} \right] - \langle \underline{\underline{\boldsymbol{\alpha}}} \rangle \delta T - \langle \underline{\underline{\boldsymbol{\xi}}} \rangle \delta\tau \right), \tag{32}$$

with δT and $\delta\tau$ being respectively the increment of temperature and of pyrolysis advancement between time t and $t + dt$. Displacement, stress and strain field are updated according to Eq. (29) by providing the appropriate initial conditions.

External load on the material are generally only of thermal origin in the problems we are considering. Boundary conditions on displacement can then take two forms:

- Fixed displacement
  $$\delta\mathbf{u} = \mathbf{0}. \tag{33}$$
- Stress free
  $$\delta\underline{\underline{\boldsymbol{\sigma}}} \cdot \mathbf{n}^{t+dt} = \mathbf{0}. \tag{34}$$

  As the small strain hypothesis holds between two close states, the unit normal $\mathbf{n}^{t+dt} \approx \mathbf{n}^t$.

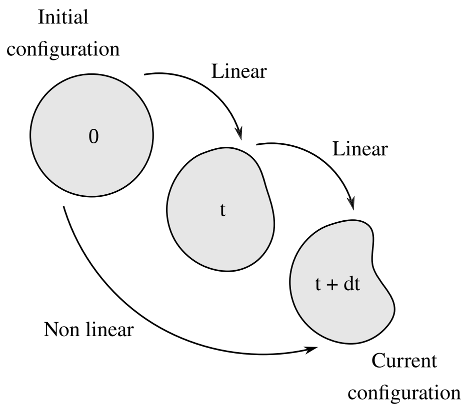

Fig. 3. Illustration of the incremental resolution.

3.2. Moving mesh strategy

As the pyromechanic model combine Eulerian and Lagrangian approaches, we use a deforming mesh technique to move the cells vertices according to the displacement at each time step. This technique is known as the Arbitrary Lagrangian–Eulerian (ALE) formulation. This allows the update of the geometry for the new reference state, including the unit normal $\mathbf{n}$. By means of the finite volume method, the integral form of a conservation equation for any variable ψ in a moving volume V bounded by a closed surface S would be for any gas or solid phase i [34]

$$\int_V \partial_t(\langle\rho_i\rangle\psi)dV + \int_V \nabla \cdot \left[\langle\rho_i\rangle(\langle\mathbf{v_i}\rangle^i - \mathbf{v_b})\psi\right] dV - \int_V \nabla \cdot \left[\langle\rho_i\rangle\Gamma_\psi \nabla\psi\right] dV$$
$$= \int_V s_\psi dV, \quad i = g, s, \tag{35}$$

where $\mathbf{n}$ is the outward pointing unit normal vector on the boundary surface S, $\mathbf{v_b}$ is the mesh velocity, Γ_ψ is the diffusion coefficient and s_ψ the volume source of ψ.

The mesh velocity corresponds to the solid velocity computed with the pyromechanic model, $\langle\mathbf{v_s}\rangle^s = \mathbf{v_b}$. Therefore, for all conservation equation involving the solid velocity $\langle\mathbf{v_s}\rangle^s$ we can write

$$\int_V \nabla \cdot \left[\langle\rho_s\rangle(\langle\mathbf{v_s}\rangle^s - \mathbf{v_b})\psi\right] dV = \mathbf{0}. \tag{36}$$

Including the mesh motion fluxes in the integral form of solid mass conservation Eq. (10) writes

$$\int_V \partial_t(\langle\rho_s\rangle)dV = -\int_V \pi_{tot} dV, \tag{37}$$

Eq. (13) for momentum-conservation equation writes,

$$\int_V \partial_t\left(\frac{\epsilon_g M_g}{R\langle T\rangle}\langle p\rangle^g\right) dV + \int_V \nabla \cdot \left(\frac{\langle p\rangle^g M}{R\langle T\rangle}\left(-\frac{1}{\mu}\underline{\underline{\mathbf{K}}}\right) \cdot \nabla\langle p\rangle^g\right) dV$$
$$= \int_V \pi^{tot} dV, \tag{38}$$

and the integral form of the energy conservation equation Eq. (27) is

$$\int_V \sum_{i\in[1,N_p]} \epsilon_i\langle\rho_i\rangle^i\langle c_{p,i}\rangle^i\partial_t\langle T\rangle dV + \int_V \partial_t\left(\epsilon_g\langle\rho_g\rangle^g\langle h_g\rangle^g - \epsilon_g\langle p_g\rangle^g\right) dV$$
$$= \int_V \left\{ \begin{array}{l} \nabla \cdot \left(\underline{\underline{\mathbf{k}}}\ \nabla\langle T\rangle\right) \\ +\nabla \cdot \left(\epsilon_g\langle\rho_g\rangle^g\langle h_g\rangle^g\left(\frac{1}{\mu}\underline{\underline{\mathbf{K}}} \cdot \nabla\langle p\rangle^g\right)\right) \\ -\sum_{i\in[1,N_p]}\langle h_i\rangle^i\partial_t(\epsilon_i\langle\rho_i\rangle^i) \end{array} \right\} dV. \tag{39}$$

The moving mesh strategy removes all dependencies on the solid velocity and only the information on the displacement $\langle\mathbf{u}\rangle^s$, computed with Eq. (31), is required. The mechanical part of the model (Eqs. (31)–(32)) has been implemented following the semi-implicit formulation described by P. Cardiff et al. [35].

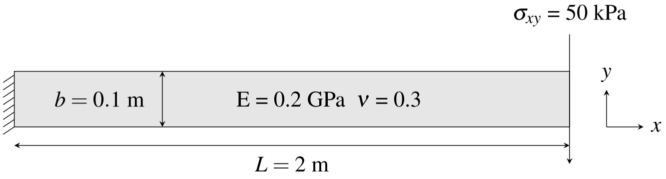

Fig. 4. Beam characteristics and boundary conditions.

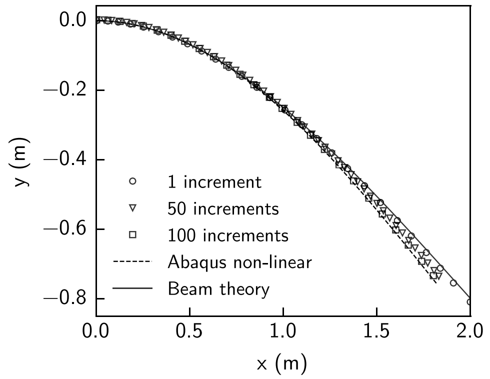

Fig. 5. Shape of the deformed center line of the beam in the $x - y$ plan for different number of increments, in comparison with beam theory and Abaqus non-linear solver.

3.3. Validation test case for the incremental approach

The aim of this section is to demonstrate that the incremental resolution allows us to describe large displacements. Usually, large displacements are solved using non-linear mechanical formulations. For this purpose, we compare the results of the incremental linear approach with a commercial non-linear finite element solver in the software Abaqus, where geometric non-linear solvers have been extensively tested. Considering the superposition principle, validating the model with a simple mechanical loading case is meaningful, as it provides insight into the overall behavior of the mass and heat transfer problem. To this end, we consider for this validation test case a simple static isotropic steel beam fixed at one end ($x = 0$) and subjected to a surface force at $x = L$ (see Fig. 4). The boundary condition is applied incrementally, with N representing the number of increments,

$$\delta\boldsymbol{\sigma} \cdot \mathbf{n} = \begin{pmatrix} 0 \\ \sigma_{xy}/N \\ 0 \end{pmatrix}, \text{ at } x = L. \tag{40}$$

During the simulation, the surface force follow the deformation. The problem is 2D with a length $L = 2$ m and width $b = 0.1$ m. A mesh convergence has led us to use 400 × 20 cells in PATO.

Fig. 5 shows the shape of the center line of the beam for different numbers of increments. A classic static resolution with 1 increment shows a good agreement with the 1D beam theory, with a slight error of 1% because of the large displacement nature of the problem. As the number of increments increases, the PATO solution tends to the non linear Abaqus one with a relative error of 3.5% for 50 increments and of 1.5% for 100 increments at the end of the beam.

4. Model applications

This section presents two applications of the pyromechanics model based on different experimental data: the first set of data originates from an experiment conducted by the authors, while the second set is taken from the literature.

4.1. Pyrolysis of a cylindrical pine wood particle

4.1.1. Experimental conditions

The conducted experiment involves a cylindrical pine sample of 19 mm diameter and 40 mm length. It is placed inside a quartz tube to ensure an inert atmosphere (N_2), and heated on its lateral surface by a resistive heater. The resistance winding was done uniformly to ensure a uniform heat flux, while extending adequately on both sides of the sample to ensure heating across the entire lateral surface. Within the sample, four 1 mm type-K thermocouples (TCs) were placed, at the midpoint of the length and at various distances from surface along the radial direction, as can be seen on Fig. 6. TC 1 was positioned at the surface and it has been attached with carbon tape to prevent any detachment. The positions of the other three thermocouples were measured using X-ray imaging. The radial distances from the surface, denoted as r_{TC2}, r_{TC3} and r_{TC4}, are such that: $r_{TC2} = 3.95$ mm, $r_{TC3} = 5.89$ mm and $r_{TC4} = 10.16$ mm. The large number of parameters required to describe the problem increases the complexity of the model. Therefore, the sample has been carefully isolated from natural convection and radiation in its longitudinal direction and the thermocouples were placed in the middle of the sample to avoid any edge effects. At the end of the experiment, the particle diameter is reduced by approximately 20%.

4.1.2. Numerical modeling of the experiment

Considering the experimental conditions, it has been chosen as a first step to modelize this experiment using a 1D-axisymmetric model in PATO to calibrate the unknown parameters. The values of the model parameters along with their method of determination are detailed in Appendix. After calibrating the parameters, the experiment was numerically modeled using a 2D-axisymmetric domain schematized in Fig. 7. In both 1D and 2D numerical simulations the thermal boundary condition is the measured temperature at TC 1. A grid size independency study conducted on both temperature and displacement showed that, except at the center for the displacement, both values converge with a minimum of 20 cells, which corresponds to a maximum cell size of 0.5 mm. To balance good resolution at the center with avoiding overly fine meshing that could lead to excessively long computation times, 62 cells were chosen for the 1D simulation, and 41 cells in the x-direction and 175 cells in the y-direction for the 2D simulation.

4.1.3. Results and discussion

The evolution of the measured and calculated temperature with the model at each thermocouple is depicted in Fig. 8(a). Additionally, Fig. 8(b) shows the model predictions in terms of temperature obtained without considering shrinkage. When considering shrinkage, the global mean relative error calculated for all thermocouples is 1.8%. However, when shrinkage is neglected, we can observe an underestimation of the temperature when 500 K is reached at each location. This phenomenon has also been observed by A. Chaurasia et al. [36]. This is because the displacements induce a shortening of the heat transfer lengths, facilitating heat diffusion across the sample. The global mean relative error calculated for all thermocouples when shrinkage is neglected is 3.4%, which means that the prediction error is 1.9 times greater in that case. Given these results, accounting for deformations helps improving the model predictions. Failing to account for shrinkage would lead to inaccurate estimate parameters such as char thermal conductivity (Fig. 9). At temperatures above 600 K, parameter calibration would result in an overestimation of char thermal conductivity to compensate for the omission of shrinkage effects.

In order to demonstrate the capabilities of the model, Fig. 10 shows the pyrolysis advancement and the longitudinal stress at different time computed with the pyromechanics model. The surface of the sample undergoes heating, pyrolysis, and shrinkage before the core. Due to the maintained cohesion between the pyrolyzed outer shell and the

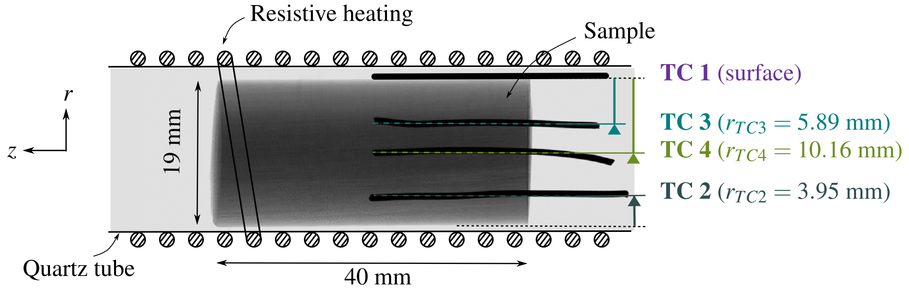

Fig. 6. 2D schematic of the experimental set up, with the radial positions r_{TC} of the thermocouples (TCs) from the surface.

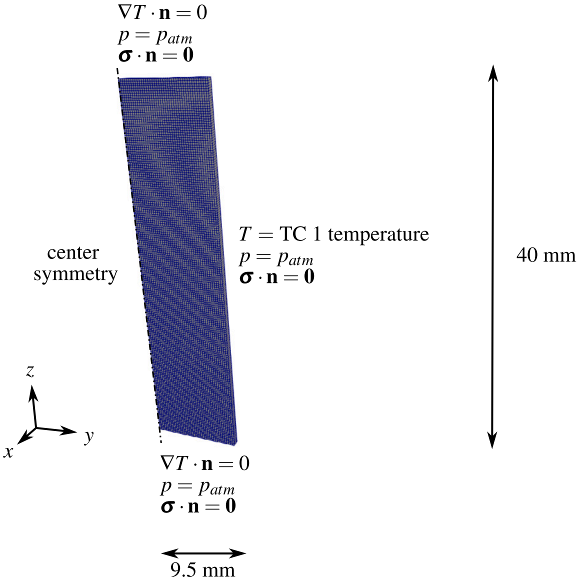

Fig. 7. 2D-axisymmetric mesh and the corresponding boundary conditions.

unpyrolyzed virgin core, the shrinking pyrolyzed shell exerts a compressive force on the virgin core. Conversely, the virgin core applies a tensile force on the pyrolyzed shell, creating a dynamic interaction between the two regions. The longitudinal stress follows the pyrolysis front during the entire process and undergoes a maximum tensile stress at the surface at about 90 s and a maximum compressive stress at the center at about 180 s.

4.2. Pyrolysis of a cylindrical beech wood particle

4.2.1. Experimental conditions

We consider in this section the experimental results of G. Gauthier and the PYRATES device [38]. The hot zone of the PYRATES device is heated by a 12 kW induction furnace, which raises the temperature of a 1 mm-thick Inconel 600 tube to a range of 500 to 1100 °C. Nitrogen gas flows through the Inconel tube. Convective and radiative heat fluxes are determined using measurements of the sample surface and furnace temperatures, coupled with numerical simulation. The temperature evolution inside the wood sample was measured using a K-type thermocouple (0.5 mm diameter). The mass of the particles during pyrolysis is determined through specific experiments. For a given pyrolysis temperature, a sample of dry biomass is pyrolyzed for a duration of Δt of two minutes. Heating is then stopped, and the sample is immediately removed from the hot zone and quenched with a nitrogen flow. Its mass is measured before a new sample is pyrolyzed for a duration of 2Δt, removed, quenched, and weighed. This process is repeated until a constant mass loss is achieved. As mentioned by G. Gauthier, the time associated with the measured mass loss is underestimated by a maximum of 20 s because the particle cools from its surface toward its core. Shrinkage is evaluated at each sample removal by measuring the maximum values of the radius or height using a caliper. By the end of the experiment, the cylindrical particle dimensions undergoes a reduction of approximately 30% of its diameter and 10% of its height.

4.2.2. Numerical modeling of the experiment

The center particle's temperature and shrinkage data obtained during the pyrolysis of a cylindrical beech wood particle of 20 mm diameter and 30 mm length at 450 °C are analyzed. The numerical results obtained by G. Gentile et al. using the bioSMOKE model [4] are compared to the pyromechanics model. This experiment is a good test case to use the full orthotropic pyromechanic model considering the dimensions of the sample and its anisotropic character. The axisymmetric hypothesis no longer holds for this case because of the orientation of the wood fibers. The 3D computational domain is represented on Fig. 11(a) along with the boundary conditions. The computational domain dimensions are chosen following the guidelines of the grid size independency study performed for the 1D and 2D meshes, i.e. with an average cell size of maximum 0.5 mm. The convective q_c and radiative q_r surface heat flux are expressed as

$$\begin{cases} q_c = h(T_s - T_\infty) \\ q_r = \varepsilon \sigma_s (T_s^4 - T_\infty^4) \end{cases} \tag{41}$$

where T_s is the surface temperature, ε the surface emissivity, h the convective coefficient and σ_s the Stefan–Boltzmann constant. The furnace temperature T_∞ is set to 468 °C, ε = 0.9 and h = 16 W m^{-2} K^{-1} as measured by G. Gauthier [38].

4.2.3. Results and discussion

Fig. 12 shows the resulting center temperature and the mass loss of the particle. As discussed in Appendix, the standard formation enthalpies have been numerically calibrated to properly describe the exothermic peak at 400 s, already observed at low pyrolysis temperatures by many authors [5,36]. This peak is attributed to the decomposition of lignin [39]. The mean relative error for the temperature is 6.2%, while for mass loss, it is 15.3%. Given the significant number of adjustable parameters involved and the uncertainties associated with the mass loss measurements, these errors are considered acceptable.

The characteristic lengths ratios (radius and length of the particle) calculated with PATO are compared to G. Gauthier measurements and bioSMOKE profiles on Fig. 13. Considering that the radius of the particle has been measured at an undetermined location, the PATO computed displacement is taken at half length. Additionally, the surface displacement is expressed in the cylindrical coordinate system represented on Fig. 11(b). As the mechanical behavior is different in the x, R and y, T directions of orthotropy, an average value of the surface displacement is used to compute the actual radius $r(t)$ of the particle. Aside from the uncertainty related to the parameters, the discrepancies between the experimental data and PATO results may be attributed to

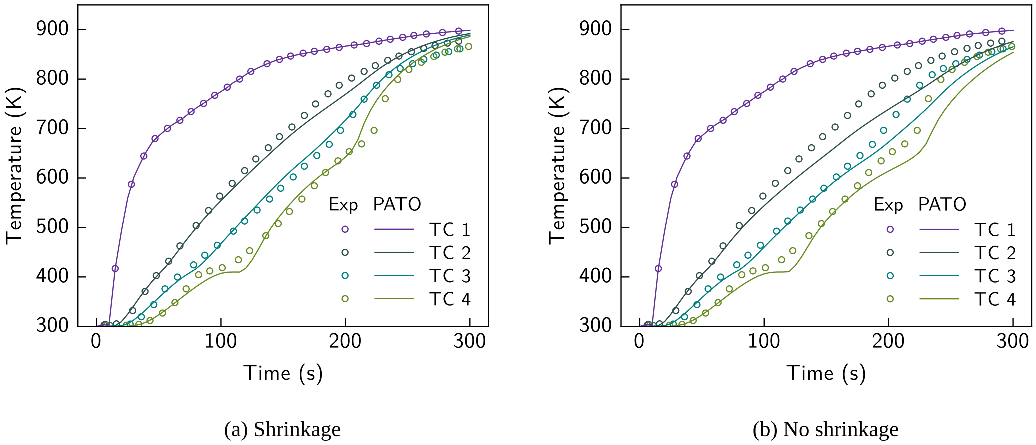

(a) Shrinkage

(b) No shrinkage

Fig. 8. Temperatures measured (∘) and calculated with PATO (—) at each thermocouple (TC) location. (a) Shrinkage is considered and (b) shrinkage is not considered.

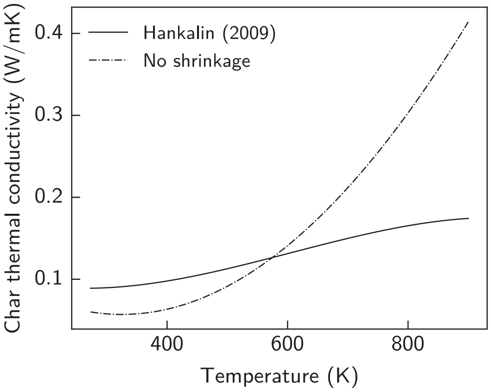

Fig. 9. Experimental measurement of char thermal conductivity [37] compared to a parameter calibration without consideration of shrinkage.

the lack of anisotropy consideration during measurements, specifically, the diameter was recorded without regard to sample orientation in the x–y plane. Considering these limitations, the mean relative errors of 3.4% for radius ratio and 1.3% for the axial length ratio are acceptable.

The comparison between bioSMOKE and PATO in Fig. 13 shows the differences between the hypotheses behind the modeling of shrinkage, as the resulting lengths variations are not the same. The results with the pyromechanics model tend to be closer to experimental results than bioSMOKE model when the devolatilization is well under way (at about 400 °C). This could be explained by the fact that neglecting internal stresses in shrinkage only models such as bioSMOKE lead to overestimate shrinkage. However, both model cannot describe the plateau and the sudden decrease of radius length between 210 s and 500 s. This could be investigated by revising the linear elasticity assumptions and extend them to material non-linearities such as plasticity behavior.

An advantage of the pyromechanics model is that it allows for the calculation of a stress field essential for analyzing failure modes and their impact on mass and heat transfer. To this end, Fig. 14(a) shows the longitudinal stress distribution σ_{zz}. As the previous numerical 2D-axisymmetric simulation, the longitudinal stress follow the pyrolysis front during the entire process. The pyrolyzed zone is tensile and the virgin zone is compressive. We give in Fig. 14(b) an overview of the 3D radial and tangential stresses distributions in comparison with the photographs of G. Gauthier [38]. As predicted, the maximum stress is higher for the radial stress as the rigidity is higher in this direction, while the shrinkage coefficient is the same for both directions. Qualitatively, we focus on the alternation of the traction in red shades and the compression in blue shades. At a given time and as the pyrolysis front progress in the particle, both radial and tangential stresses are compressive in the virgin core. The tensile nature of the radial stress at the surface may explain the longitudinal cracking shown from 240 s on Fig. 14(d).

5. Conclusion

This study presented a 3D anisotropic pyromechanics model coupling pyrolysis kinetics, heat and mass transfer and stress/strain distributions. The model uses volume averaging to derive heat, mass, and momentum conservation equations for porous materials composed of gas and solid phases. The compatibility between the displacement calculation and the transient thermal problem, and the consideration of large displacements during pyrolysis, were addressed through a numerical incremental approach and a moving mesh strategy. The main assumption is that the pyromechanics model assumes that pyrolysis shrinkage arises from three contributions: elastic, thermal and pyrolysis deformations. A first experimental comparison highlighted the importance of considering shrinkage in the numerical calibration of parameters. The second experimental comparison served as a reference to compare the pyromechanics model assumptions on deformation with a model from the literature.

At this stage, a first key advantage of the pyromechanics model lies in its physical framework, which effectively captures the effect of internal stresses on the overall deformation—a capability that provides a basis for future research into cracking phenomena. A second key advantage is that, unlike isotropic or 2D models, it captures directional dependencies and internal stress distributions in any kind of particle geometry. However, the model's dependency on extensive material property data presents a limitation, which may not always be readily available. A simple kinetic scheme was used in this work, but coupling this model with a detailed competitive pyrolysis mechanism (such as the one of E. Ranzi et al. [40]) could enable its application at the particle scale to simulate conversion processes like gasification and optimize conditions for specific biomass pyrolysis products, such as hydrogen or biochar.

Several promising research directions emerge. The integration of in-situ microtomography could offer real-time insights into morphological changes by retrieving the deformation field during conversion and comparing it to the model predictions. Furthermore, investigating the causes of cracking and incorporating damage mechanics would significantly extend the model's applicability across fields such as thermochemical conversion. Future work should prioritize refining experimental methods to identify intrinsic material properties and extending the model to address cracking and plasticity behavior. Its practical applications range from improving the design of pyrolysis reactors to enhancing the efficiency of biomass conversion processes.

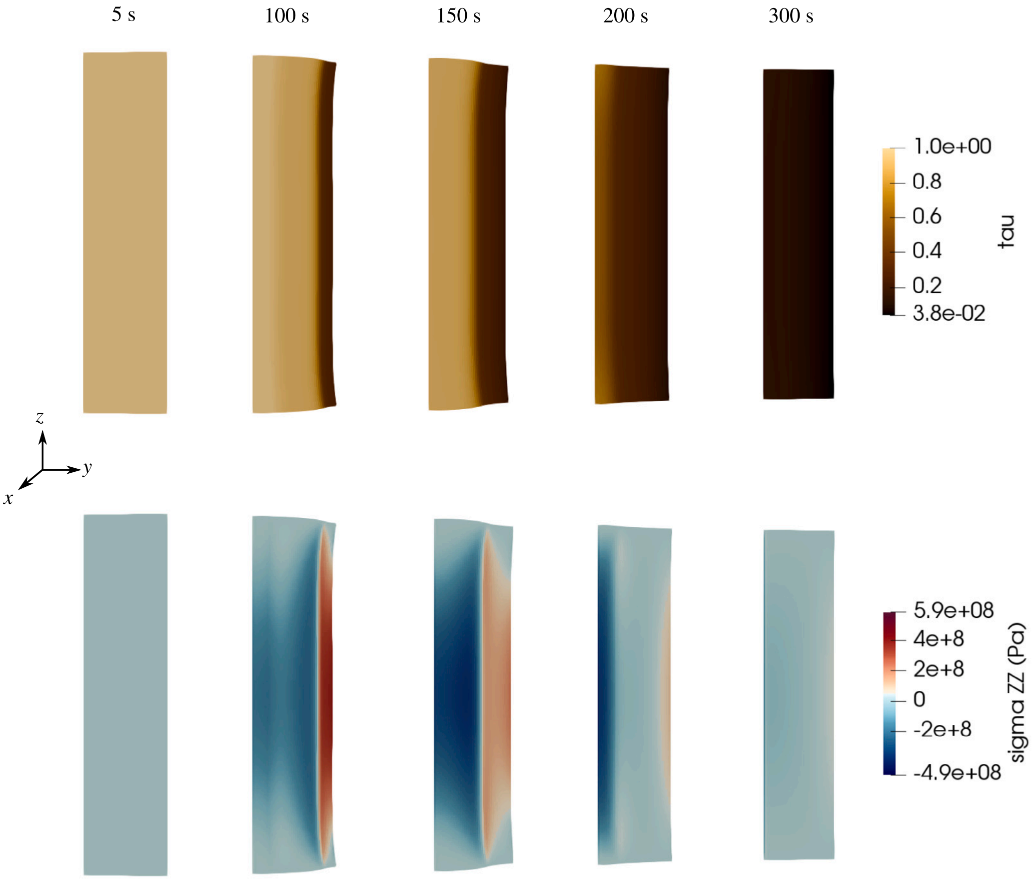

Fig. 10. Average pyrolysis advancement τ and longitudinal stress σ_{zz} in the 2D-axisymmetric particle for various times.

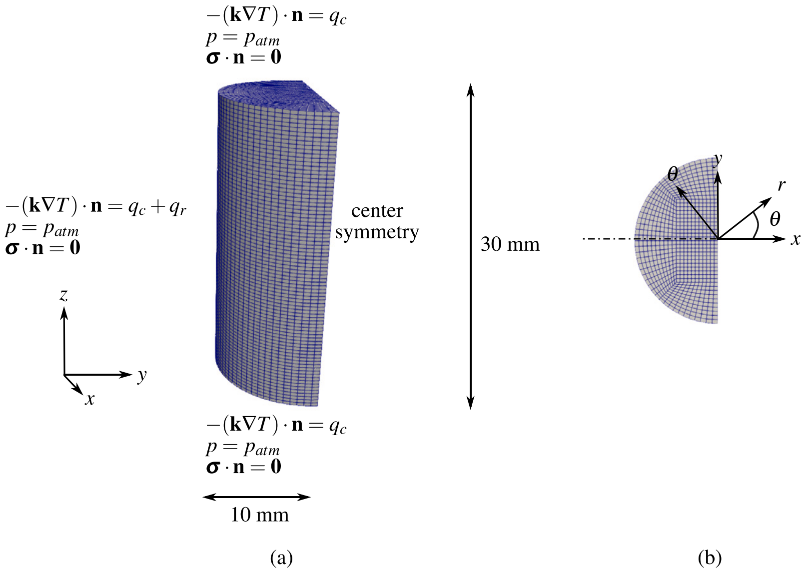

Fig. 11. (a) 3D computational domain and associate boundary conditions and (b) Mesh in the $x-y$ plan and cylindrical coordinate system.

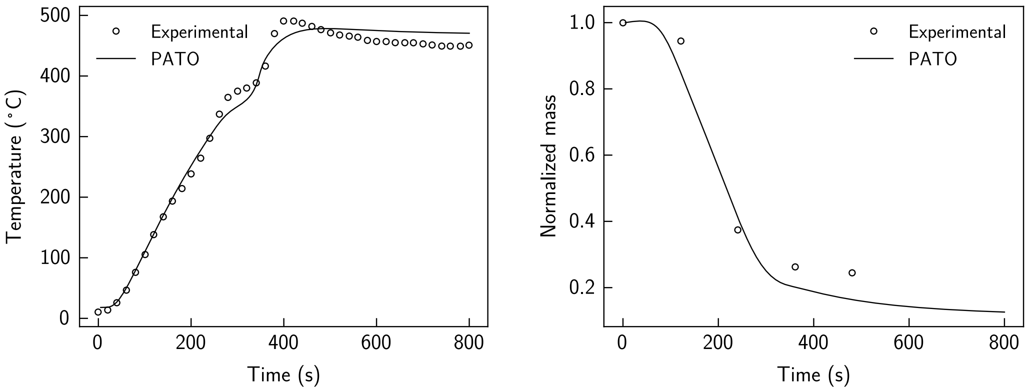

(a)

(b)

Fig. 12. Temporal evolution of (a) the center temperature and (b) the mass in a beech wood cylindrical particle. Experimental data come from [38].

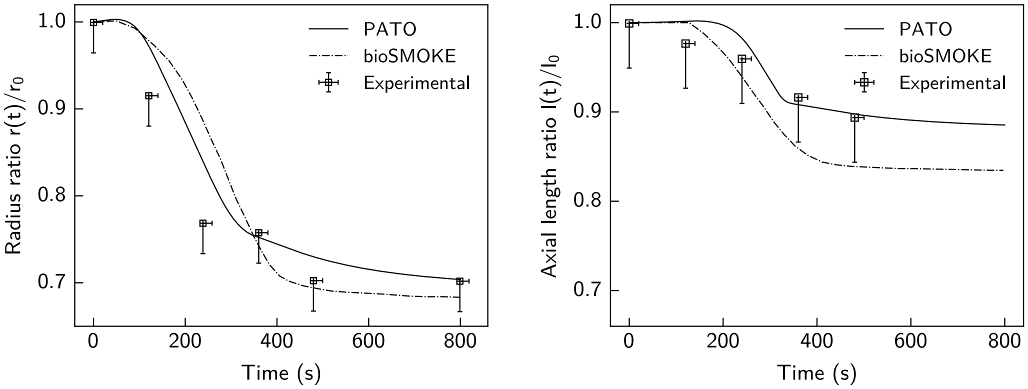

(a)

(b)

Fig. 13. (a) Temporal evolution of (a) the radius and (b) the axial length of the cylindrical particle. Experimental data come from G. Gauthier [38] and bioSMOKE profiles from [4].

CRediT authorship contribution statement

Flora Lahouze: Writing – original draft, Software, Methodology, Investigation, Formal analysis, Data curation. **Wahbi Jomaa:** Writing – review & editing, Validation, Supervision, Methodology, Conceptualization. **Cyrille Métayer:** Investigation, Data curation, Conceptualization. **Michaël Meyer:** Investigation, Data curation, Conceptualization. **Francesco Panerai:** Investigation, Data curation, Conceptualization. **Jean Lachaud:** Writing – review & editing, Validation, Supervision, Methodology, Conceptualization.

Declaration of competing interest

The authors declare that they have no known competing financial interests or personal relationships that could have appeared to influence the work reported in this paper.

Acknowledgment

This research was funded, in whole or in part, by the French National Research Agency (ANR) under the project ANR-22-CE51-0014-01.

Appendix. Parameters estimation

A.1. *Pyrolysis parameters*

The choice has been made to use a simple kinetic scheme for describing the pyrolysis process to minimize the unknowns in the problem. A thermogravimetric analysis (TGA) at 10 K/min has been conducted in inert atmosphere (N_2) measuring the mass loss during the pyrolysis of the maritime pine wood sample of experiment 1. The Arrhenius parameters for a four-component reaction scheme listed in Table A.1 were calibrated using the FiTGA algorithm [41]. The mass loss rate is correctly reproduced (Fig. A.15). Even though the calibration is done on only one heating rate, the values are in the range of literature data, which are themselves often highly variable [42]. The mass loss fraction $\mathcal{F}_{ij}$ and standard formation enthalpies $h_{f,ij}$ have been numerically calibrated on temperature measurements using a genetic algorithm implemented in the Sandia National Laboratories Dakota software [43]. Intrinsic volume fraction have been determined based on literature data for maritime pine (*Pinus Pinaster*). It has been assumed that pine wood, classified as a softwood, consists of approximately 40%–50% cellulose by weight, 25%–35% hemicellulose, and 16%–33% lignin, with a total average density ranging between 450 and 650 $\mathrm{kg\,m^{-3}}$ [44,45].

(a) Longitudinal stress σ_{zz} (Pa)

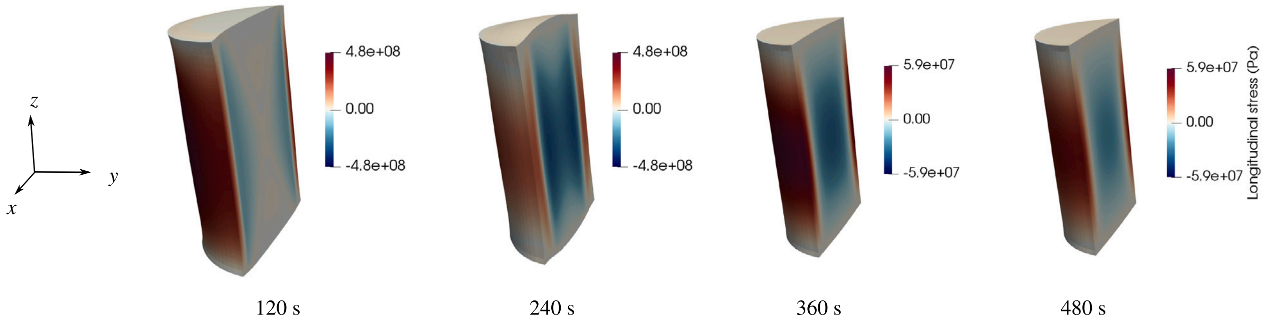

(b) Radial stress σ_{yy} (Pa)

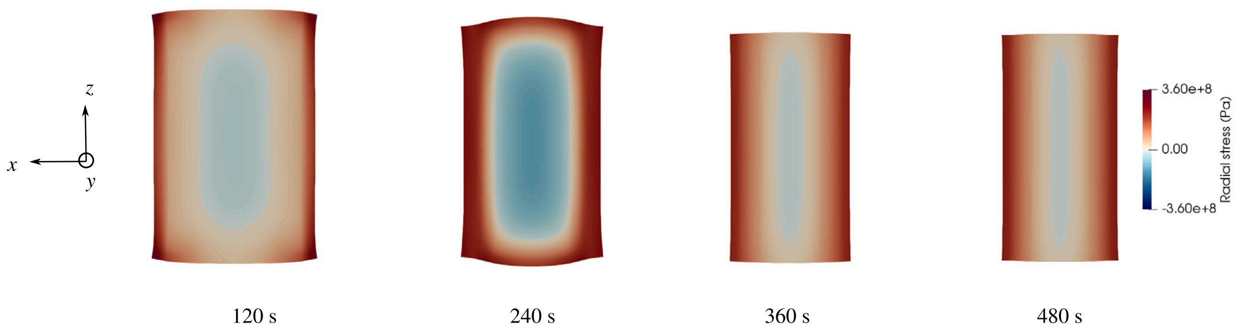

(c) Tangential stress σ_{xx} (Pa)

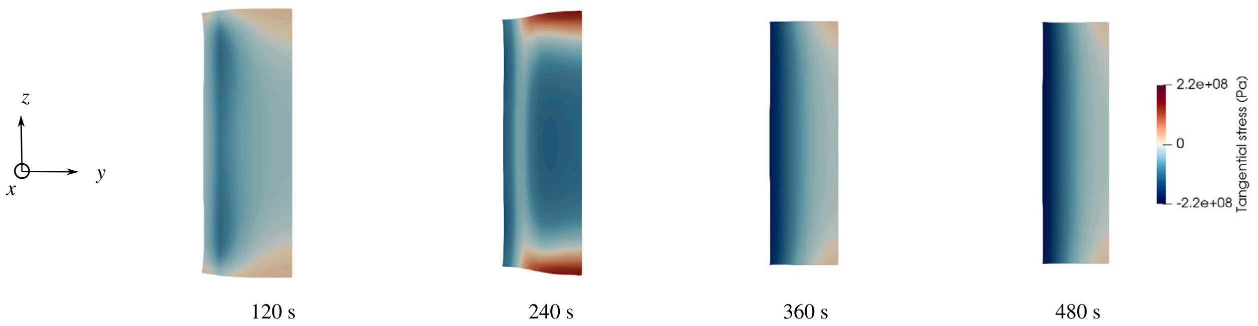

(d) Experimental data

Fig. 14. Morphological evolution of the wood particle compared to experimental data at a pyrolysis temperature of 450 °C [38]. (a) Longitudinal stress, (b) Radial stress, (c) Tangential stress at different times and (d) Experimental data from [38]. Blue shades denote compression and red shades are for traction. (For interpretation of the references to color in this figure legend, the reader is referred to the web version of this article.)

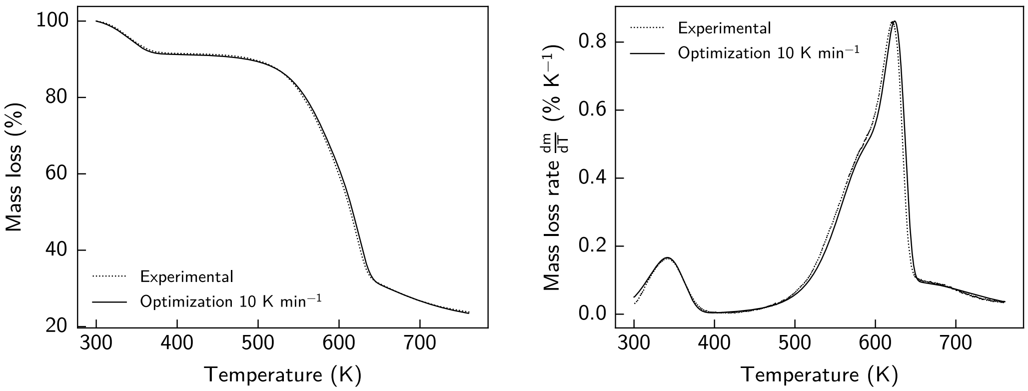

(a) (b)

Fig. A.15. (a) Mass loss and (b) Mass loss rate obtained with thermogravimetric analysis on a maritime pine wood sample at 10 K/min.

Table A.1
Summary of the pyrolysis parameters used for both pine and beech sample, along with their method of determination.

Parameters	Water	Hemicellulose	Cellulose	Lignin	Method of determination
$\mathcal{A}_{i1}$ (s^{-1})	1.48×10^4	1.17×10^7	9.56×10^{17}	1.802	Calibrated on TGA
$\mathcal{E}_{i1}$ (J mol^{-1})	41 300	102 521	237 194	37 118	Calibrated on TGA
$\mathcal{F}_{i1}$ (–)	1	0.68	0.66	0.80	Calibrated on Experiment 1
Pine wood sample					
$h_{r,ij}$ (kJ/kg)	−2270	−600	−600	−600	Calibrated on Experiment 1
ϵ_i	0.03	0.09	0.13	0.11	Literature [44,45]
$\langle \rho_i \rangle^i$ (kg m^{-3})	1000	1500	1500	1500	Literature [46]
Beech wood sample					
$h_{r,ij}$ (kJ/kg)		−154	−752	−106	Calibrated on Experiment 2
ϵ_i		0.14	0.1913	0.1167	Literature [38]
$\langle \rho_i \rangle^i$ (kg m^{-3})		1500	1500	1500	Literature [46]

For the beech wood sample used in the second experiment, the modeling of the experiment in [38] involves a competitive mechanism for describing pyrolysis kinetics, so the parameters are not applicable for the parallel scheme used in this work. As mentioned in [38], the beech sample is dried and the same kinetic and thermodynamic parameters for a three-component reaction scheme are used. The intrinsic volume fractions are calculated from a beech composition analysis made in [38]. The value are listed in Table A.1.

A.2. Thermo-physical properties

The thermo-physical parameters are all computed as a function of the conversion as

$$\phi = \tau\phi_v + (1-\tau)\phi_c, \tag{A.1}$$

for any parameters ϕ, subscript v is for *virgin* and subscript c is for *char*.

According to V. Hankalin et al. [37], the thermal capacity varies little depending on the wood species, but rather with temperature and moisture content.

The thermal conductivity is modeled as a third order polynomial

$$k_i = k_{i,1} + k_{i,2}T + k_{i,3}T^2 + k_{i,4}T^3, \quad i = v, c. \tag{A.2}$$

The char thermal conductivity is assumed to be 0.09 W m^{-1} K^{-1} at 309 K, increasing approximately to 0.145 W m^{-1} K^{-1} at 673 K and to 0.175 W m^{-1} K^{-1} at 923 K [37]. It is also assumed to be lower than the virgin thermal conductivity. These informations lead to solve a system of equations for the expression of char conductivity k_c given in Table A.2. The undetermined parameters at this stage are the virgin thermal conductivity and the formation enthalpies. The calibration strategy involves fixing the coefficients of the virgin thermal conductivity following the guidelines of V. Hankalin et al. [37] : the radial virgin thermal conductivity of pine ranges between 0.15 and 0.18 W m^{-1} K^{-1} at 309 K and there is a 5 % increase in thermal conductivity between 309 K and 370 K for pine with a density of 455 kg m^{-3}. The longitudinal thermal conductivity is taken to be 1.9 times greater for all temperatures [37,38]. The virgin and char parameters are given in Table A.2.

Table A.2
Thermo-physical properties of virgin and char states.

Property	Direction	Virgin	Char
c_p (kJ kg^{-1} °C^{-1})[a]		$2.3 - 1.15\exp(-5.5 \times 10^{-3}T)$	$4.7256 \times 10^{-10}T^3$ $-1.3099 \times 10^{-6}T^2$ $+1.6027 \times 10^{-3}T + 1.0629$
$\underline{\underline{\mathbf{k}}}$ (W m^{-1} K^{-1})[b]	longitudinal	$1.9 \times k_{v,trans}$	$1.9 \times k_{c,trans}$
	Tangential	$0.157 + 10^{-5}T$ $+10^{-9}T^2 + 1.9 \times 10^{-11}T^3$	$0.139 - 4.15 \times 10^{-4}T$ $+10^{-6}T^2 - 5.53 \times 10^{-10}T^3$
$\underline{\underline{\mathbf{K}}}$ (m^2)[c]	Longitudinal	10^{-14}	10^{-12}
	Tangential	10^{-15}	10^{-13}

[a] Measurements on beech wood [38].
[b] Estimation based on measurements on pine wood [37].
[c] Estimation based on [12].

A.3. Mechanical properties

Wood is known to be an anisotropic material but the symmetry of the wood structure allows us to describe this material as an orthotropic one, with three axes of symmetry. We consider the longitudinal axis (L, z), the radial axis (R, y) and the tangential axis (T, x). The three

Table A.3
Thermo-mechanical properties in the orthotropic coordinate system (Longitudinal, Radial, Transversal) [20,47,49].

Property	Directions			Method of determination
	L	R	T	
Young modulus E (MPa)	11 000	1243	858	Literature [47]
Thermal expansion tensor $\underline{\underline{\alpha}}$ (K^{-1})	4×10^{-6}	2.5×10^{-5}	3.4×10^{-5}	Literature [20,49]
Pyrolysis shrinkage tensor $\underline{\underline{\xi}}$ (–) (**Pine wood**)	0.1	0.2	0.2	Calibrated on Experiment 1
Pyrolysis shrinkage tensor $\underline{\underline{\xi}}$ (–) (**Beech wood**)	0.12	0.34	0.34	Calibrated on Experiment 2
	Plans			
	LT	LR	TR	
Shear modulus G (MPa)	891	902	143	Literature [47]
Poisson coefficient ν (–)	0.292	0.328	0.362	Literature [47]

young modulus, the three shear modulus and the six Poisson coefficients have been found in the literature [47] for pine wood and used in all numerical simulation.

According to F.F.P. Kollmann and W.A. Côté [48], the tangential thermal expansion coefficient is in general greater than in the radial direction. Parallel to the grain, i.e. in the longitudinal direction, Kollmann and Côté report that the thermal expansion coefficient varies little with the wood species and is very small in front of the two others directions.

The pyrolysis shrinkage tensors for both pine and beech sample have been numerically calibrated on experiments 1 and 2 respectively. According to K. Davidsson [13], for an anisotropic particle, the overall longitudinal shrinkage is between 5%–25% and always smaller than the tangential (25%–40%) and radial overall shrinkage (15%–40%), depending on the type of wood. The thermo-mechanical properties are listed in Table A.3.

Data availability

Data will be made available on request.

References

[1] Saidur R, Abdelaziz E, Demirbas A, Hossain MS, Mekhilef S. A review on biomass as a fuel for boilers. Renew Sustain Energy Rev 2011;15(5):2262–89.

[2] Bryden KM, Hagge MJ. Modeling the combined impact of moisture and char shrinkage on the pyrolysis of a biomass particle. Fuel 2003;82:1633–44.

[3] Di Blasi C. Heat, momentum and mass transport through a shrinking biomass particle exposed to thermal radiation. Chem Eng Sci 1996;51:1121.

[4] Gentile G, Debiagi PEA, Cuoci A, Frassoldati A, Ranzi E, Faravelli T. A computational framework for the pyrolysis of anisotropic biomass particles. Chem Eng J 2017;321:458–73.

[5] Di Blasi C. Modeling chemical and physical processes of wood and biomass pyrolysis. Prog Energy Combust Sci 2008;34:47–90.

[6] Baroudi D, Ferrantelli A, Li KY, Hostikka S. A thermomechanical explanation for the topology of crack patterns observed on the surface of charred wood and particle fibreboard. Combust Flame 2017;182:206–15.

[7] Wang S, Ding P, Lin S, Huang X, Usmani A. Deformation of wood slice in fire: Interactions between heterogeneous chemistry and thermomechanical stress. Proc Combust Inst 2021;38:5081–90.

[8] Henderson J, Wiecek T. A mathematical model to predict the thermal response of decomposing, expanding polymer composites. J Compos Mater 1987;21(4):373–93.

[9] Villermaux J, Antoine B, Lede J, Soulignac F. A new model for thermal volatilization of solid particles undergoing fast pyrolysis. Chem Eng Sci 1986;41:151–7.

[10] Babu BV, Chaurasia AS. Heat transfer and kinetics in the pyrolysis of shrinking biomass particle. Chem Eng Sci 2004;59:1999–2012.

[11] Larfeldt J, Leckner B, Melaaen MC. Modelling and measurements of the pyrolysis of large wood particles. Fuel 2000;79(13):1637–43.

[12] Hagge MJ, Bryden KM. Modeling the impact of shrinkage on the pyrolysis of dry biomass. Chem Eng Sci 2002;57(14):2811–23.

[13] Davidsson KO, Pettersson JBC. Birch wood particle shrinkage during rapid pyrolysis. Fuel 2002;81:263–70.

[14] Sánchez M, Maya JC, Pecha B, Chejne F, Quinchía-Figueroa AM. Effect of particle characteristics, kinetics and transport phenomena on the prediction of particle mass loss and products yields during biomass fast pyrolysis. J Anal Appl Pyrolysis 2022;168:105786.

[15] Pecha MB, Thornburg NE, Peterson CA, Crowley MF, Gao X, Lu L, Wiggins G, Brown RC, Ciesielski PN. Impacts of anisotropic porosity on heat transfer and off-gassing during biomass pyrolysis. Energy Fuels 2021;35(24):20131–41.

[16] Li F, Wu K, Yang K, Ge Z, Feng J, Zhang H. A comprehensive pyrolysis model for lignocellulosic biomass particles with a special emphasis on the anisotropic characteristics. Fuel 2023;341:127635.

[17] Bellais M. Modelling of the pyrolysis of large wood particles (Ph.D. thesis), KTH; 2007.

[18] Blondeau J, Jeanmart H. Biomass pyrolysis in pulverized-fuel boilers: Derivation of apparent kinetic parameters for inclusion in CFD codes. Proc Combust Inst 2011;33(2):1787–94.

[19] Cueff G, Mindeguia JC, Dréan V, Breysse D, Auguin G. Experimental and numerical study of the thermomechanical behaviour of wood-based panels exposed to fire. Constr Build Mater 2018;160:668–78.

[20] Sreekanth M, Prasad BVSSS, Kolar AK, Thunman H, Leckner B. Stresses in a cylindrical wood particle undergoing devolatilization in a hot bubbling fluidized bed. Energy Fuels 2008;22:1549–59.

[21] Wang J, Ku X, Liu Z. Three-dimensional simulation of the pyrolysis of a thermally thick biomass particle. Energy Fuels 2023;37:4413–28.

[22] Shen D, Gu S, Luo KH, Bridgwater A. Analysis of wood structural changes under thermal radiation. Energy Fuels 2009;23(2):1081–8.

[23] Hastaoglu MA, Kahraman R, Syed MQ. Pellet breakup due to pressure generated during wood pyrolysis. Ind Eng Chem Res 2000;39:3255–63.

[24] Lachaud J, Mansour NN. Porous-material analysis toolbox based on openfoam and applications. J Thermophys Heat Transfer 2014;28(2):191–202.

[25] Lachaud J, Scoggins J, Magin T, Meyer M, Mansour N. A generic local thermal equilibrium model for porous reactive materials submitted to high temperatures. Int J Heat Mass Transfer 2017;108:1406–17.

[26] Montanari C, Olsén P, Berglund LA. Sustainable wood nanotechnologies for wood composites processed by in-situ polymerization. Front Chem 2021;9:682883.

[27] Biot MA. Theory of elasticity and consolidation for a porous anisotropic solid. J Appl Phys 1955;26(2):182–5.

[28] Whitaker S. Flow in porous media III: deformable media. Transp Porous Media 1986;1:127–54.

[29] Jomaa W, Puiggali J. Drying of shrinking materials: Modellings with shrinkage velocity. Drying Technol 1991;9(5):1271–93.

[30] Perré P, May B. A numerical drying model that accounts for the coupling between transfers and solid mechanics. Case of highly deformable products. Dry Technol 2001;19(8):1629–43.

[31] Demirdžić I, Horman I, Martinović D. Finite volume analysis of stress and deformation in hygro-thermo-elastic orthotropic body. Comput Methods Appl Mech Engrg 2000;190(8–10):1221–32.

[32] Blondeau J, Jeanmart H. Biomass pyrolysis at high temperatures: Prediction of gaseous species yields from an anisotropic particle. Biomass Bioenergy 2012;41:107–21.

[33] Chateauneuf A. La méthode des éléments finis – calcul non-linéaire géométrique. Tech l'Ingén Superstruct Bâtiment 2016;base documentaire : TIP253WEB(ref. article : c6003).

[34] Jasak H, Tukovic Z. Automatic mesh motion for the unstructured finite volume method. Trans FAMENA 2006;30(2):1–20.

[35] Cardiff P, Karač A, Ivanković A. A large strain finite volume method for orthotropic bodies with general material orientations. Comput Methods Appl Mech Engrg 2014;268:318–35.

[36] Chaurasia A, Kulkarni B. Most sensitive parameters in pyrolysis of shrinking biomass particle. Energy Convers Manage 2007;48(3):836–49.

[37] Hankalin V, Ahonen T, Raiko R. On thermal properties of a pyrolysing wood particle. In: Finnish-Swedish flame days 2009, January 28-29, 2009, Naantali, Finland. 2009, p. 16.

[38] Gauthier G. Synthèse de biocarburants de deuxième génération : étude de la pyrolyse à haute température de particules de bois centimétriques (Theses), Ecole des Mines d'Albi-Carmaux; 2013.

[39] Di Blasi C, Branca C, Galgano A. On the experimental evidence of exothermicity in wood and biomass pyrolysis. Energy Technol 2017;5(1):19–29.

[40] Ranzi E, Cuoci A, Faravelli T, Frassoldati A, Migliavacca G, Pierucci S, Sommariva S. Chemical kinetics of biomass pyrolysis. Energy Fuels 2008;22(6):4292–300.

[41] Torres-Herrador F, Leroy V, Helber B, Contat-Rodrigo L, Lachaud J, Magin T. Multicomponent pyrolysis model for thermogravimetric analysis of phenolic ablators and lignocellulosic biomass. AIAA J 2020;58:4081–9.

[42] D'Antoni J, Ben-Abdelwahed A, Gaborieau C, Duphil A, Jomaa W, Lachaud J. Biomass pyrolysis: Thermodynamic parameters review and determination through TGA. In: 37th international conference on efficiency, cost, optimization, simulation and environmental impact of energy systems. Rhodes, Greece: ECOS 2024; 2024, p. 2042–53.

[43] Adams BM, Bohnhoff WJ, Dalbey KR, Ebeida MS, Eddy JP, Eldred MS, Hooper RW, Hough PD, Hu KT, Jakeman JD, et al. Dakota, a multilevel parallel object-oriented framework for design optimization, parameter estimation, uncertainty quantification, and sensitivity analysis: version 6.13 user's manual. Tech. rep., Albuquerque, NM (United States): Sandia National Lab. (SNL-NM); 2020.

[44] Park C, Atreya A, Baum HR. Experimental and theoretical investigation of heat and mass transfer processes during wood pyrolysis. Combust Flame 2010;157:481–94.

[45] Saavedra Flores EI, de Souza Neto EA, Pearce C. A large strain computational multi-scale model for the dissipative behaviour of wood cell-wall. Comput Mater Sci 2011;50.

[46] Kellogg R, Sastry C, Wellwood R. Relationships between cell-wall composition and cell-wall density. Wood Fiber Sci 1975;170–7.

[47] Laboratory FP. Wood handbook—wood as an engineering material. General technical report FPL-gTR-282, Madison, WI: U.S. Department of Agriculture, Forest Service, Forest Products Laboratory; 2021, p. 543.

[48] Kollmann FFP, Côté WA. Principles of wood science and technology : I solid wood. Springer Berlin Heidelberg; 1968, p. 592.

[49] Bodig J, Jayne B. Mechanics of wood and wood composites. Van Nostrand Reinhold; 1982.